

Electrochemical Generation of High-Valent Oxo-Manganese Complexes Featuring an Anionic N5 Ligand and Their Role in O—O Bond Formation

Sachidulal Biswas,¹ Srijan Narayan Chowdhury,¹ Panjo Lepcha,¹ Subhankar Sutradhar,² Abhishek Das,² Tapan Kanti Paine,*² Satadal Paul,*³ and Achintesh N. Biswas*¹

¹ Department of Chemistry, National Institute of Technology Sikkim, Ravangla, South Sikkim 737139, India

² School of Chemical Sciences, Indian Association for the Cultivation of Science, 2A and 2B Raja S.C. Mullick Road, Jadavpur, Kolkata 700032, India.

³ Department of Chemistry, Bangabasi Morning College, Kolkata, West Bengal 700009, India

* Corresponding authors: Achintesh N. Biswas: achintesh@nitsikkim.ac.in; Tapan Kanti Paine: ictkp@iacs.res.in; Satadal Paul: satadal2008@gmail.com

ABSTRACT

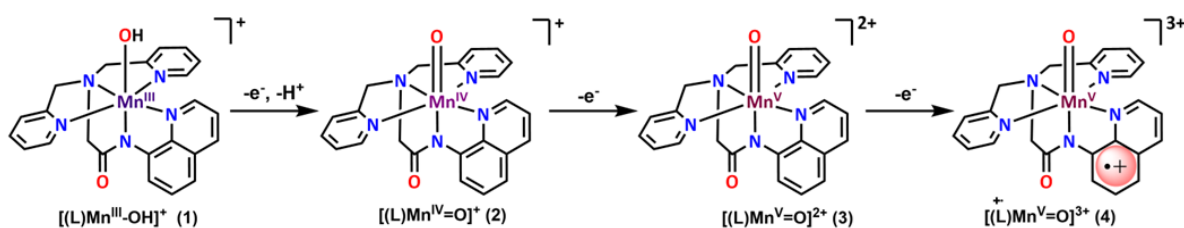
Generation of high-valent oxomanganese complexes through controlled removal of protons and electrons from low-valent congeners is a crucial step toward the synthesis of functional analogues of the native oxygen evolving complex (OEC). In-depth studies of the water oxidation activity of such biomimetic compounds help to understand the mechanism of O—O bond formation presumably occurring at the last step of the photosynthetic cycle. Scarce reports of reactive high-valent oxomanganese complexes underscores the impetus for the present work, wherein we report the electrochemical generation of the non-heme oxomanganese(IV) species, [(dpaq)Mn^{IV}(O)]⁺ (**2**), through a proton-coupled electron transfer (PCET) process from the hydroxomanganese complex [(dpaq)Mn^{III}(OH)]ClO₄ (**1**). Controlled potential spectroelectrochemical studies of **1** in wet acetonitrile at 1.45 V vs. NHE revealed quantitative formation of **2** within 10 min. The high-valent oxomanganese(IV) transient exhibited remarkable stability and could be reverted to the starting complex (**1**) by switching the potential to 0.25 V vs. NHE. The formation of **2** *via* PCET oxidation of **1** demonstrates an alternate pathway for the generation of the oxomanganese(IV) transient (**2**) without the requirement of redox-inactive metal ions or acid additives as proposed earlier. Theoretical studies predict that one-electron oxidation of [(dpaq)Mn^{IV}(O)]⁺ (**2**) forms a manganese(V)-oxo (**3**) species, which can be oxidized further by one-electron to a formally manganese(VI)-oxo transient (**4**). Theoretical analyses suggest that the first oxidation event (**2** to **3**) takes place at the metal-based *d*-orbital whereas, in the second oxidation process (**3** to **4**), the electron eliminates from an orbital composed of equitable contribution from metal and ligand, leaving a single electron in the quinoline-dominated orbital in the doublet ground spin state of the manganese(VI)-oxo species (**4**). This mixed metal- ligand (quinoline)-based oxidation is proposed to generate a formally Mn(VI) species (**4**), a non-heme analogue of the species ‘compound I’, formed in the catalytic cycle of cytochrome P-450. We propose that the highly electrophilic species **4** catches water during cyclic voltammetry experiments and results in O—O bond formation leading to electrocatalytic oxidation of water to hydrogen peroxide.

Introduction

Proton-coupled electron transfer (PCET) reactions play vital role in sequential oxidations of the biological oxygen evolving complex (OEC) resulting in the $4e^-/4H^+$ oxidation of water to dioxygen during photosynthesis.¹⁻⁴ The reaction, involving the removal of four electrons from two molecules of water and the formation of O—O bond, offers several mechanistic puzzles, some of which, have been unearthed by extensive research efforts.⁵ The OEC featuring a tetranuclear cluster ($CaMn_4O_5$) is oxidized by the tyrosine radical, $TyrO^\bullet$ (Y_z^\bullet) through a series of PCET processes to generate a putative oxomanganese(V) species that reacts with water to install an O—O bond.⁶⁻⁸ Unlike the ubiquitous route for the formation of oxometal transients in biology *via* two-electron reductive activation of dioxygen,^{9,10} oxomanganese(V) species in OEC is formed following one electron, one proton oxidations of the corresponding Mn-aqua and Mn-hydroxo complexes.¹¹⁻¹³ In the realm of biomimetic chemistry, oxometal complexes are typically engendered through the reaction of reduced metal complexes with oxygen-transfer agents, such as peracids, iodosylarenes, or hydrogen peroxide.¹⁴⁻¹⁶ However, facile access to high-valent metal-oxo intermediates following electrons/protons transfers from their low-valent congeners and monitoring their reactivity with water can provide important insights into the O—O formation process and thus, aid the development of efficient functional mimics of OEC. Therefore, light weight metal complexes with terminal hydroxo/aqua ligands are potential target catalysts for sunlight-driven water oxidation.¹⁷ Several oxometal complexes generated by PCET from the corresponding aqua-/hydroxo-bound metal precursors have been demonstrated to play key roles in electrochemical water oxidation.¹⁸⁻²⁴ Electrochemically generated oxo-transients have also been shown to be active in the oxygenation of C—H bonds.²⁵⁻²⁷ Most of these studies have focused on the electrochemical oxidation of reduced Fe—OH₂/Fe—OH complexes.²⁸⁻³² In contrast, PCET reactivity of manganese complexes has been significantly less explored.³³⁻³⁷ Previously, we reported the formation of a manganese(IV)-oxo complex (**2**) bearing a pentadentate ligand H-dpaq (H-dpaq = 2-[bis(pyridin-2-ylmethyl)]amino-*N*-quinolin-8-yl-acetamide) from the precursor manganese(III)-hydroxide complex (**1**) *via* stepwise proton and electron transfer.³⁷

Interestingly, the electronic spectrum of **2** shares a striking similarity with that reported for a redox-inactive metal bound oxo-transient, [(dpaq)Mn^{IV}(O)]⁺-Mⁿ⁺ (**2-Mⁿ⁺**, Mⁿ⁺ = redox-inactive metal ion) supported by the same ligand.³⁸ Moreover, ¹⁸O isotope labelling studies confirmed that the O-atom in **2** originates from the manganese(III)-OH congener, though the claim has recently been questioned.³⁹ In a recent communication, Nam and co-workers have shown the generation of an acid-bound Mn(IV)-oxo complex, {[(dpaq)Mn^{IV}(O)]-HOTf}⁺ by treating **1** with PhIO in presence of HOTf at 298 K.⁴⁰ The species has been comprehensively characterized by various spectroscopic tools. Upon crystallization, the authors obtained the crystal structure of the corresponding Mn(IV)-OH complex, [(dpaq)Mn^{IV}(OH)](OTf)₂, which was shown to revert to the acid-bound oxomanganese(IV) upon dissolution. These interesting developments regarding the ability of the oxomanganese(IV) complex to

bind protons or redox-inactive metal ions led us to revisit the high-valent chemistry of the Mn–dpaq system. We have focused our investigation on the electrochemistry of $[(\text{dpaq})\text{Mn}^{\text{III}}(\text{OH})]^+$ and its oxomanganese derivatives. We reasoned that the apparent dichotomy regarding the source of oxygen atom in the high-valent oxomanganese(IV) complex (**2**) and the requirement of additives (protons/redox-inactive metal ions) in its formation can be sorted out by generating the putative species in a non-aqueous medium, thereby circumventing the use of any external chemical oxidants. Therefore, efforts have been devoted to the electrochemical generation of the oxo transient in acetonitrile, aiming to obtain the ‘unbound’ $[(\text{dpaq})\text{Mn}^{\text{IV}}(\text{O})]^+$ (**2**). Herein, we report the successful electrochemical generation of **2** from its precursor complex (**1**) in acetonitrile, achieving a yield of over 90% through controlled potential electrolysis. The formation of **2** from **1** electrochemically confirms that the oxomanganese(IV) transient (**2**) can indeed be achieved without employing any additives. High-valent manganese complexes formed following further electrochemical oxidations of **2** could not be spectroscopically characterized, presumably owing to their very high reactivity. However, quantum chemical computations based on Density Functional Theory (DFT) and multireference wave function-based methods suggest that these oxidations involve a metal-centered and a mixed metal-ligand centered redox processes to generate a manganese(V)-oxo (**3**) and a formally manganese(VI)-oxo transient (**4**), respectively (Scheme 1).



Scheme 1. Electrochemically generated oxomanganese transients

Finally, electrocatalytic water oxidation by complex **1** in acetonitrile–water has been studied. Based on the experimental and theoretical investigations, we show that the electrocatalytic oxidation of water by the hydroxomanganese(III) complex (**1**) in acetonitrile favors the $2e^-/2\text{H}^+$ pathway to yield hydrogen peroxide. Overall, the present study contributes to the advancement of our understanding of high-valent oxomanganese complexes bearing the pentadentate amidate ligand (dpaq), offering new perspective on their formation.

Results and discussion

Electrochemical oxidation of **1**

Previous studies have confirmed that the hydroxomanganese(III) complex (**1**) exists in equilibrium with the μ -oxodimanganese(III,III) complex in acetonitrile.⁴¹ The speciation depends on the amount of water

and only a trace amount of water is sufficient to shift the equilibrium towards the monomeric complex. Therefore, the cyclic voltammetry (CV) experiment of complex **1** was performed in acetonitrile containing 100 equivalents of water. CV of 0.2 mM **1** using a glassy carbon working electrode exhibit a redox couple at $E_{1/2} = 1.33$ V vs. NHE (Figure 1 and Figure S1). Scanning towards more anodic potentials resulted in additional oxidation events centred at $E_{p,a} = 1.58$ and 1.9 V vs. NHE. CV experiments of complex **1** in 0.2 M borate buffer confirmed that the Mn^{III}/Mn^{IV} redox wave shifts cathodically with increasing pH. The E -pH plot reveals a slope of -70 mV/pH, which is notably close to the theoretical value of 59 mV/pH suggested by the Nernst equation corresponding to a one electron transfer process coupled with the transfer of a proton. This finding aligns well a proton coupled electron transfer (PCET) process reported earlier (Figure S2).⁴² Thus, the redox event at $E_{1/2} = 1.33$ V vs. NHE is attributed to the oxidation of the hydroxomanganese(III) complex, $[(dpaq)Mn^{III}(OH)]^+$ (**1**) to oxomanganese(IV) complex $[(dpaq)Mn^{IV}(O)]^+$ (**2**).

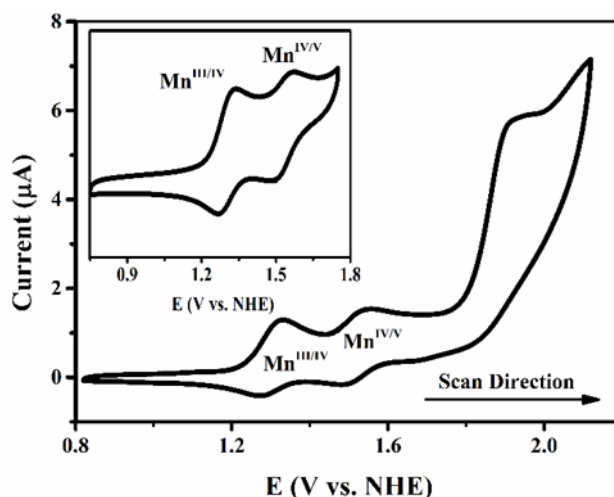


Figure 1. CV of 0.1 mM complex **1** in acetonitrile and 150 mM water containing 0.1 M $LiClO_4$ as the supporting electrolyte at a scan rate of 10 mV/s at 293 K. Working electrode = glassy carbon (GC), reference, and counter electrode = Pt. Inset shows the first two redox couples in acetonitrile.

To further support the formation of the $[(dpaq)Mn^{IV}(O)]^+$ intermediate, detailed spectroelectrochemical study of **1** was carried out in a quartz cell using a Pt gauze working electrode, $Ag/AgCl$ (satd. KCl) as the reference electrode and Pt wire as the counter electrode at 298 K. A CV scan from 0.25 V to 1.75 V vs. NHE at a scan rate of 2 mV/s was performed in wet acetonitrile with simultaneous acquisition of UV-visible spectra at 1.0 s interval. During the anodic sweep, we could observe the formation of absorption features at 700 and 500 nm (Figure 2a, 2b). The final electronic spectrum was found to be in perfect congruence with the previously reported spectrum for the oxomanganese(IV) transient, $[(dpaq)Mn^{IV}(O)]^+$ (**2**) (Figure 2a).³⁷

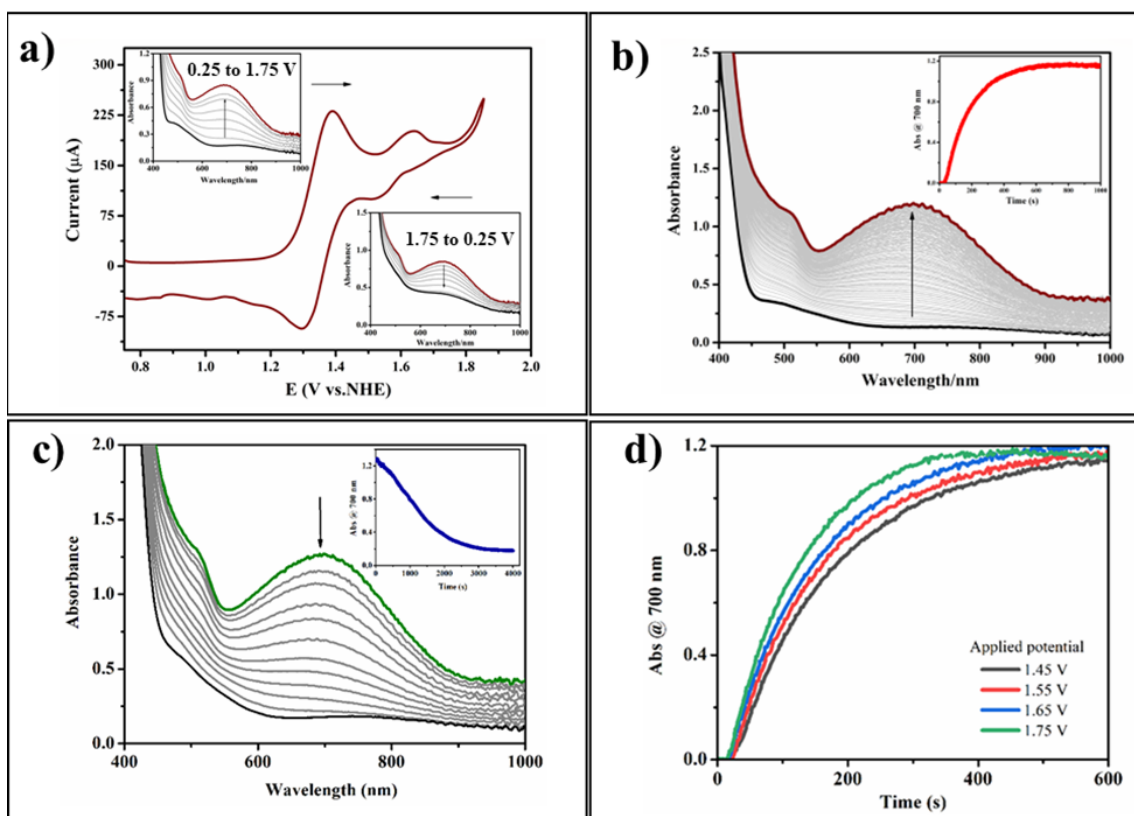


Figure 2. (a) CV of complex **1** (1.0 mM) in wet acetonitrile at a scan rate of 2 mV/s; inset shows the change in the UV-vis spectra of **1** during a CV scan from 0.25 to 1.75 V (top left) and from 1.75 V to 0.25 V (bottom right). (b) UV-vis spectra showing the formation of **2** during the electrolysis of an acetonitrile solution of complex **1** (0.5 mM) at a potential 1.45 V vs. NHE. Inset shows the change in absorbance at 700 nm with time of electrolysis. (c) Decay of **2** upon switching the potential to 0.25 V. (d) Formation of **2** during the electrolysis of an acetonitrile solution of complex **1** (0.5 mM) at different applied potentials. All the data were recorded at 293 K. WE = Pt gauze, CE = Pt and RE = Ag/AgCl (satd. KCl).

The results, therefore, confirm the generation of **2** from the PCET oxidation of **1** and the yield of **2** was determined to be greater than 90% at 298 K. The bands at 700 and 500 nm decayed during the reverse scanning, but the electronic feature of the starting complex (**1**) was not fully restored (Figure 2a). The oxidized species showed remarkable stability at 1.45 V ($t_{1/2} = 2$ h at 298 K). Switching the potential to 0.25 V vs. NHE resulted in the decay of the absorption bands. However, the reduction of **2** to **1** was found to be slow as it took 45 min for quantitative reduction of **2** to **1** (Figure 2c). Further spectroelectrochemical studies were performed to monitor the electronic spectral changes associated with the conversion of **1** to **2** as a function of the applied potential. As shown in Figure 2d, the application of a potential greater than 1.4 V vs. NHE resulted in the formation of the oxomanganese(IV) transient as judged by the appearance of the absorption bands at 700 nm and 500 nm. For unambiguous characterization, controlled potential electrolysis (CPE) experiments were conducted on **1** using a large-surface-area porous carbon electrode (PCE) or fluorine doped tin oxide (FTO) electrode in wet

acetonitrile. Application of a potential of 1.45 V resulted in the formation of a pale green species **2** from a golden yellow solution of **1** within 5 min (Figures S3).

To further confirm the presence of a Mn(IV)-oxo complex, Raman spectroscopic studies were carried out. The ^{18}O -labelled hydroxo complex was prepared by purging $^{18}\text{O}_2$ into a solution of the Mn(II) precursor complex in acetonitrile.³⁷ The corresponding ^{16}O (**2- ^{16}O**) and ^{18}O (**2- ^{18}O**) labelled oxomanganese(IV) complexes were prepared by controlled potential electrolysis of the hydroxomanganese complexes (**1- ^{16}OH** and **1- ^{18}OH**). The Raman spectrum of **2- ^{16}O** measured with 532 nm laser excitation showed a band at 803 cm^{-1} , which shifted to 775 cm^{-1} upon ^{18}O substitution for **2- ^{18}O** (Figure 3). The isotopic shift of 28 cm^{-1} agrees well with the calculated value for a Mn-O diatomic harmonic oscillator based on Hooke's law. The ν_{MnO} value (803 cm^{-1}) is higher than that reported for the proton-bound (793 cm^{-1}) and Sc^{3+} bound (795 cm^{-1}) oxomanganese(IV) complex,⁴⁰ indicating a stronger manganese oxygen bond in the electrochemically generated **2**. The results are consistent with the presence of an 'unbound' Mn(IV)O unit in **2** rather than a H^+ or metal-bound oxomanganese(IV) complex, since Lewis-acidic additives would have pulled electrons away from the manganese-oxygen double bond making it weaker.⁴⁰ It is worth noting that in the previous study, we reported the generation of **2** by treating the hydroxomanganese(III) complex (**1**) with O-transfer agents in presence of acid additives. the Raman spectrum of the complex drop-casted on a glass slide exhibited a Mn-O band at 682 cm^{-1} . A recent study has elucidated that the oxomanganese(IV)-oxo complex (**2**) in its solidified form tends to acquire a proton, thereby undergoing a swift transformation into the corresponding hydroxomanganese(IV) complex. As recently demonstrated, the oxomanganese(IV)-oxo complex (**1**) takes up a proton during solidification and rapidly gets converted to the corresponding hydroxomanganese(IV) complex.⁴⁰ Hence, the Raman spectrum previously reported for the solid state of complex **2** essentially corresponds to the Mn(IV)-OH complex, and the observed Mn-O band at 682 cm^{-1} is a characteristic feature of this species in its solid state.

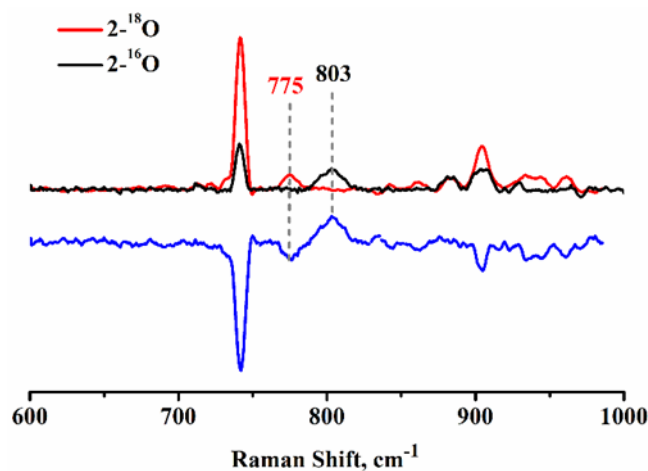


Figure 3. Raman spectra of electrochemically generated $[(\text{dpaq})\text{Mn}^{\text{IV}}(\text{O})]^+$ (**2**) intermediates (**2- ^{16}O** black line and **2- ^{18}O** red line) obtained upon excitation at 532 nm at 293 K. Blue line shows the difference between the spectra of **2- ^{16}O** and **2- ^{18}O** .

Bulk electrolysis experiments at 1.45 V in the presence of excess water were also carried out to ascertain the source of the O-atom in **2**. The addition of large excess of water during bulk electrolysis experiments had no positive effect on the rate of formation of **2** (Figure S4). Moreover, the oxo transient (**2**) was formed at a lower yield in the presence of large excess of water (Figure S4). Additional CPEs at different potentials using either large surface-area porous carbon electrode (PCE) or FTO working electrodes of varying surface area confirmed that the rate of electrochemical generation of **2** is a function of the applied potential and the surface area of the working electrode. Two possible scenarios seem to be in line with the experimental findings. Firstly, the formation of the oxomanganese(IV) complex (**2**) from the hydroxomanganese(III) precursor (**1**) *via* a proton coupled electron transfer (PCET) process can explain the zero-order dependence of the rate of formation of **2** on the concentration of water. Alternatively, the results can also be rationalized by considering a rapid water exchange process, thereby making the rate-determining step independent of water concentration. However, we could not detect any ^{18}O -labelled **2** by ESI-MS after adding H_2^{18}O after its complete generation. In fact, addition of water to **2** in acetonitrile led to a much faster decay of the oxo-transient. A lower yield of **2** in the presence of additional water and its decay following the addition of water may indicate the ability of the oxo-transient in forming O—O bond. The results prove that complex **2** does not undergo water exchange and the oxygen atom in **2** is solely derived from the hydroxo congener (**1**) and not from water. To further support this, we allowed the electrochemically generated oxomanganese(IV) complex to react with thioanisole in the presence and absence of H_2^{18}O . Analysis of the reaction products by GC-MS revealed the formation of the corresponding sulfoxide with no incorporation of isotopically labelled oxygen (Figure S5a). However, when thioanisole was reacted with the isotopically **2**- ^{18}O generated from the **1**- ^{18}OH complex, 41% incorporation of labelled oxygen into the sulfoxide product was observed (Figure S5b). We argue that apart from the trace amount of water needed for the electrochemical generation of **2** (*vide infra*) to shift the equilibrium of the Mn(III)-hydroxo and μ -oxodimanganese(III,III) complex in acetonitrile towards the monomeric complex, water does not play any role in the electrochemical formation of **2** from **1**. Consequently, this study presents an alternative route for the formation of $[(\text{dpaq})\text{Mn}^{\text{IV}}(\text{O})]^+$ (**2**), circumventing the requirement for redox-inactive metal ions or acid additives.

After successfully identifying the redox pairs in the first oxidation event, we proceed further to characterize the redox events at 1.58 and 1.9 V vs. NHE (Figure 1). The redox event at 1.58 V can be tentatively assigned to the formation of an oxomanganese(V) species. The third oxidation wave centred at 1.9 V vs. NHE in acetonitrile may be either due to a metal-based or ligand-based oxidation. The redox non-innocence of the H-dpaq ligand has already been reported earlier in case of electrocatalytic water oxidation by the $[\text{Co}(\text{dpaq})\text{Cl}]\text{Cl}$ and oxygen reduction by $[\text{Cu}(\text{dpaq})]\text{ClO}_4$.^{21,43} Thus, to gain insight into these redox events, CVs of $[\text{Zn}^{\text{II}}(\text{dpaq})]^+$ and the free H-dpaq ligand were recorded in acetonitrile under otherwise identical conditions. As shown in Figure S6, the Zn(II) complex and the free ligand display irreversible oxidation waves at $E_{p,a} = 1.5$ V and 1.7 V vs. NHE, respectively. The

results confirm the non-innocent role of the ligand in the oxidation process of **1** and we argue that the third oxidation event generates a formally manganese(VI) intermediate (**4**) *via* ligand-centred oxidation. The current height of this oxidation wave is significantly larger than that expected for a one-electron oxidation event and is likely to be associated with the oxidation of the small amount of water present in the reaction medium (*vide supra*). Thus, the experimental results indicate the formation of an oxomanganese(V) cation radical species, a non-heme analogue of ‘compound I’ formed in the catalytic cycle of cytochrome P-450.^{44, 45} Attempts were also made to generate complex **3** and **4** by bulk electrolysis in acetonitrile. However, despite our best efforts the oxidized species could not be generated by bulk electrolysis. Instead, the CPE experiments led to the formation of the pale green species **2**, albeit at lower yields. This observation suggests the heightened reactivity and correspondingly shorter half-lives of the oxidized intermediates within the experimental conditions, as compared to the relatively stable **2**.

Electronic structure of the high-valent manganese-oxo species

The formation of the high-valent oxomanganese complexes (**2**, **3** and **4**) following electrochemical oxidation of the hydroxomanganese(III) complex (**1**) was further studied by quantum chemical computations based on Density Functional Theory (DFT) and multireference wave function-based methods. Geometry optimization of complex **2** and its oxidized species (**3** and **4**) in different possible spin states established quartet, singlet, and doublet ground spin states for **2**, **3**, and **4**, respectively (Figure 4 and Table S1). Theoretical calculation of the oxidation potentials for the oxidation events $[(\text{dpaq})\text{Mn}^{\text{IV}}\text{O}]^{1+}/[(\text{dpaq})\text{Mn}^{\text{V}}\text{O}]^{2+}$ and $[(\text{dpaq})\text{Mn}^{\text{V}}\text{O}]^{2+}/[(\text{dpaq})\text{Mn}^{\text{VI}}\text{O}]^{3+}$ yielded the values 1.66 V and 2.20 V (Table S2), which are within 0.1 – 0.3 V error margin with respect to the experimental values (see experimental section). Stability check of the wave functions of **2**, **3** and **4** showed instabilities in the wave-function of **3**, indicating multireference character of wave function. Hence, the geometry of compound **3** is reoptimized following stabilization of the wave function. Scrutiny of the quasi-restricted orbitals in complex **2** reveals the singly occupied molecular orbitals (SOMO) as manganese - d_{xy} , d_{xz} and d_{yz} orbitals as expected. In the one-electron oxidized state, the axial bonds in **3** get compressed (Table 1), which in turn increases the interaction among the Mn, axial ligand, and quinoline-based orbitals (Figure 5).

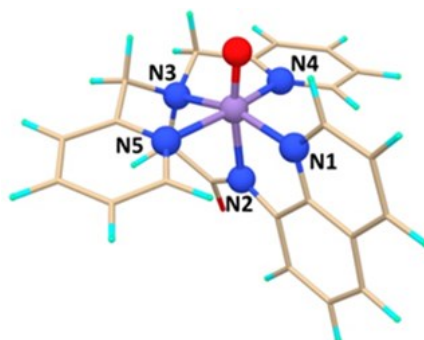


Figure 4. Schematic of the $[(\text{dpaq})\text{MnO}]^{n+}$ complexes ($n = 1, 2 \& 3$ for **2**, **3** & **4**, respectively). Colour code: Purple – Mn, Red – O, Blue – N, Grey – C, Cyan – H.

Table 1. Comparison of bond lengths (Å) in **2**, **3** and **4**. Refer to Figure 3 for atom labels.

	2	3	4
Mn – O	1.69	1.57	1.57
Mn – N1	1.99	1.99	1.96
Mn – N4	2.03	2.02	2.01
Mn – N3	2.03	2.01	2.01
Mn – N5	2.03	2.02	2.01
Mn – N2	2.01	1.97	1.99

The strong metal-ligand interactions also force the complex to adopt a low-spin state by pushing both the electrons into the d_{xy} orbital (Figures 5 and 6). Evolution of relative energy ordering of DFT-derived MOs through **2** to **3** to **4** is shown in Figure S7. However, in complex **4**, the Mn – N2 axial bond is slightly elongated than those in **3**, which can be explained by the occupancy of corresponding metal-ligand antibonding orbitals. To understand these structural changes, the multiconfigurational Complete Active Space Self Consistent Field (CASSCF) calculation was performed. From the set of DFT-derived quasi-restricted orbitals, the manganese d_{z^2}, d_{yz}, d_{xz} orbitals in bonding and antibonding combinations with the p_z, p_y and p_x orbitals of axial oxygen (labelled as σ_1, π_1, π_2 and $\sigma_1^*, \pi_1^*, \pi_2^*$ respectively), the bonding and antibonding orbitals between manganese $d_{x^2-y^2}$ and the equatorial ligands (σ_2 and σ_2^* respectively), and the d_{xy} orbital of manganese (labelled as η) were chosen to form the active space for CASSCF calculation in case of complex **2**.

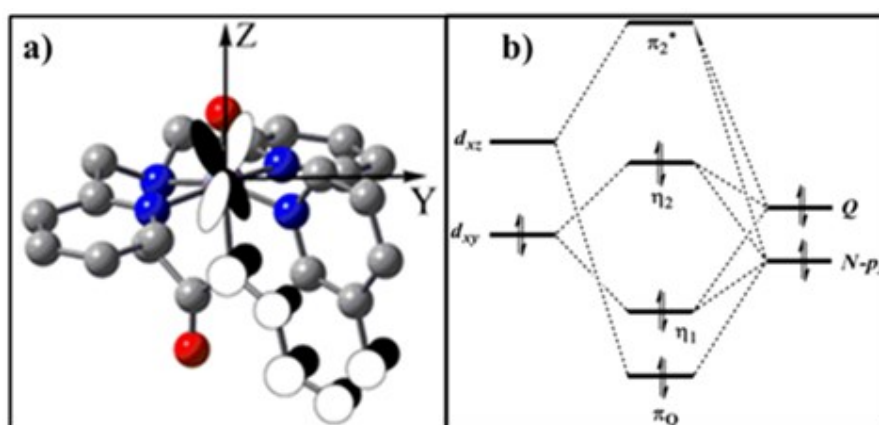


Figure 5. (a) Interaction among the metal and ligand orbitals and (b) electronic distribution in the resulting MOs.

This computational set-up has been validated through a reasonable match between the experimental and simulated optical absorption spectra (Figure S8). The experimental 500 nm and 700 nm spectral peaks has been assigned to the electronic transition to the σ_1^* and σ_2^* orbital from π_1^* / π_2^* orbitals, respectively. The CAS (11,9) calculation on the complex **2** results in

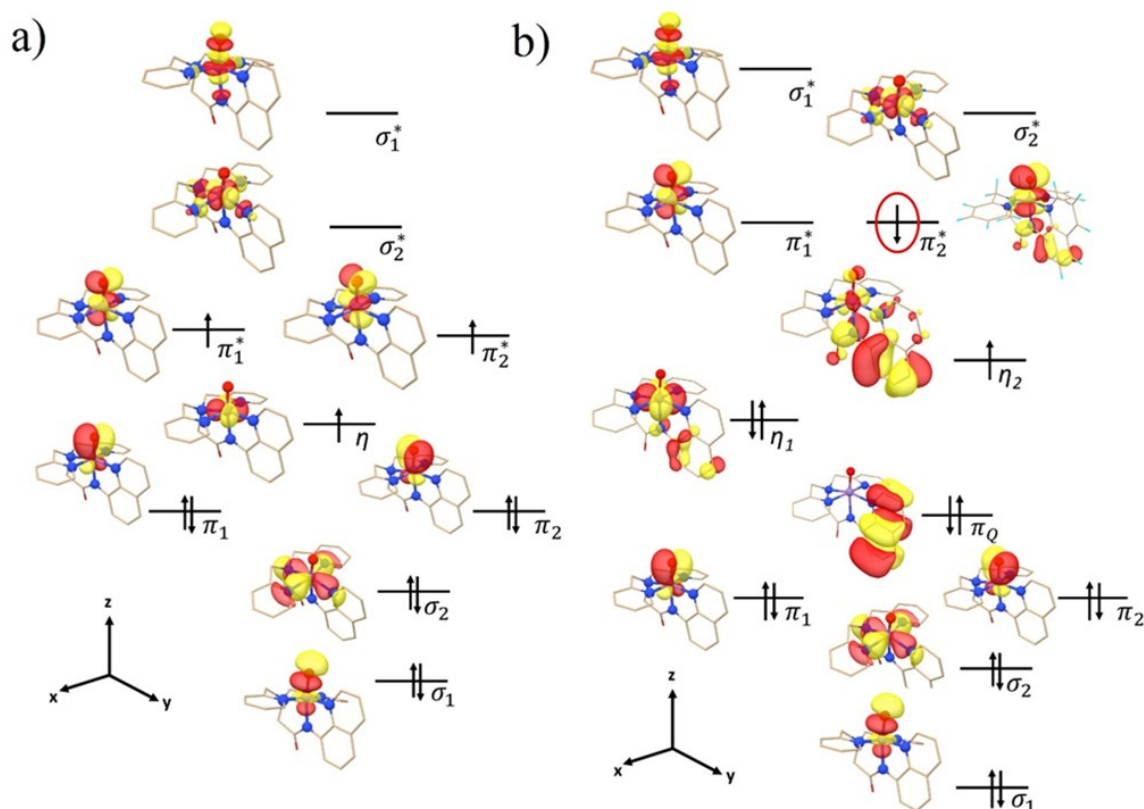


Figure 6. Electronic distribution in the natural orbitals obtained through CASSCF calculation on the (a) complex **2** with CAS(11,9) active space and the (b) complex **3** with CAS(14,11) active space. In the one electron oxidation of the complex **3**, the encircled electron is eliminated to form the doublet ground spin state of the complex **4**. (Only the dominant configurations are considered in the schematics).

electronic distribution as shown in the Figure. 6a, where the manganese based π_1^* , π_2^* and η are identified as SOMOs. However, tetragonal compression in the oxidized forms (*cf.* Table 1), *i.e.*, in complexes **3** and **4**, consequences a strong interaction among manganese-based d -orbitals (d_{xz} and d_{xy}), the p_x orbital of axial anionic nitrogen (N2 in Figure 4) and the quinoline-based π orbital (referred to as Q in Figure 5). This π -type interaction between Mn- d_{xy} and anionic nitrogen based p_x orbital is further facilitated by the non-linearity of the axial bond ($\angle O - Mn - N2 = 174^\circ$). This interaction among four orbitals gives rise to four molecular orbitals as shown in the Figure 5b and labelled as π_Q , η_1 , η_2 and π_2^* respectively, which accommodate six electrons, of which two are originating from the metal-based d_{xy} -orbital and four from the anionic nitrogen and quinoline-based π orbital. The maximum contribution towards the MO π_Q comes from the quinoline-based π orbital. The η_1 orbital is mainly constituted from the d_{xy} orbital, while the quinoline-based π and the N2 based p_x orbital are the major components in the η_2 orbital (The composition and distinct images of η_1 and η_2 are given in Scheme S1). The additional two MOs (π_Q and η_2), arising due to a strong interaction between metal and ligand orbitals as a result of tetragonal compression, are included in the CASSCF calculation for complexes **3** and **4**, where the active space for CASSCF calculation is expanded to (14,11). Inspection of the natural orbitals obtained from CAS(14,11) calculation reveals an multireference character for complex **3**, since its

singlet ground state wave function $|\psi\rangle_s^3$ is found to be the combination of two dominant configuration state functions as follows,

$$|\psi\rangle_s^3 = 0.57|\sigma_1^2\sigma_2^2\pi_1^2\pi_2^2\pi_Q^2\eta_1^1\eta_2^1\pi_1^{*0}\pi_2^{*1}\sigma_2^{*0}\sigma_1^{*0}\rangle + 0.17|\sigma_1^2\sigma_2^2\pi_1^2\pi_2^2\pi_Q^2\eta_1^2\eta_2^2\pi_1^{*0}\pi_2^{*0}\sigma_2^{*0}\sigma_1^{*0}\rangle.$$

In the major configuration which constitutes 57% of the ground state wave function, one unpaired electron resides in the quinoline-based η_2 orbital, whereas the other unpaired electron is housed in the metal- d_{xz} dominated π_2^* orbital with significant contribution from anionic nitrogen and quinoline. The spins of these two unpaired electrons orient antiparallel to each other to represent the singlet ground state since the CASSCF calculation provides a spin-reserved solution. Hence the dominant (57%) configuration represents an open-shell character, and the second major configuration (17%) bears a closed – shell character. The dominant configuration, showing one down-spin in the metal- d_{xz} dominated π_2^* orbital, one up-spin in the quinoline-based η_2 orbital and doubly occupied η_1 orbital, which is mainly constituted from the d_{xy} orbital define the metal as a d^3 system. Hence, the system can be considered to have the down-spin electron in the metal- d_{xz} dominated π_2^* orbital antiferromagnetically coupled with the quinoline based up-spin electron resulting in a spin singlet state in the spin-adapted MCSCF calculation. Hence, the formally Mn(V)-oxo species can better be represented as Mn(IV)($\uparrow\downarrow\downarrow$) – Quinoline (\uparrow) representing a physical oxidation state IV of the metal center (arrows represent up-/down- spin). At this point, this is to mention that the multiconfigurational nature of the ground state for complex **3** as supported by the co-existence of two configurations (57% and 17%) in the CASSCF result could not be detected by the DFT. The singlet complex **3** turns into the doublet complex **4** through one-electron oxidation, and thus an active space of (13,11) is chosen for the CASSCF calculation on complex **4**. The resulting solution represents multiconfigurational character for the doublet ground state $|\psi\rangle_d^4$ of complex **4**, which can be described as follows.

$$|\psi\rangle_d^4 = 0.42|\sigma_1^2\sigma_2^2\pi_1^2\pi_2^2\pi_Q^2\eta_1^2\eta_2^1\pi_1^{*0}\pi_2^{*0}\sigma_2^{*0}\sigma_1^{*0}\rangle + 0.12|\sigma_1^2\sigma_2^2\pi_1^2\pi_2^2\pi_Q^2\eta_1^1\eta_2^1\pi_1^{*0}\pi_2^{*1}\sigma_2^{*0}\sigma_1^{*0}\rangle.$$

Comparison of the dominant configurations in $|\psi\rangle_s^3$ and $|\psi\rangle_d^4$ clearly demonstrates that the oxidation process involves electron removal from the metal- d_{xz} dominated π_2^* orbital, leaving the single unpaired electron on the quinoline dominated η_2 orbital. However, as per the other configuration, complex **4** may also have three SOMOs. This electronic distribution in the doublet ground state of **4** is reflected in its spin density, which is dispersed on the anionic nitrogen, quinoline and the metal (Figure 7). At this point, this is to note that a similar kind of non-innocent behaviour of the quinoline-based π orbitals has earlier been reported for a Cu–complex.⁴³ From the facts and figures as could be found in ref. 43 and the present work, it can be concluded that the presence of an anionic ligand facilitates the interaction between the metal-based d -orbitals and the π -orbitals based on quinoline-donor, and thus triggers ligand non-innocence.

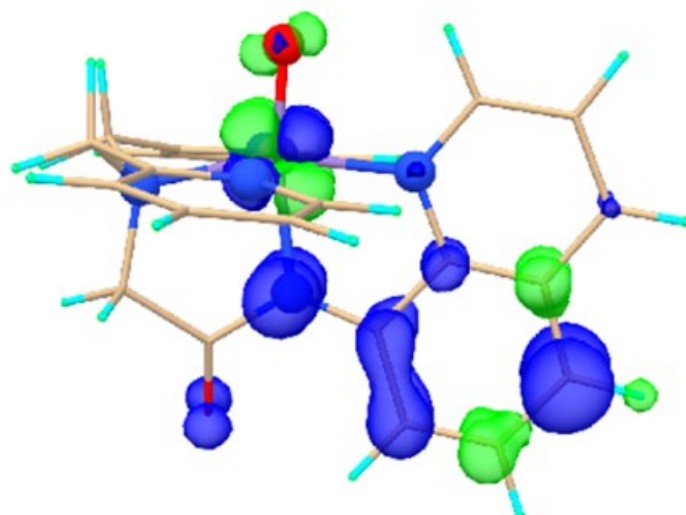


Figure 7. Spin density distribution in complex **4**.

Electrocatalytic water oxidation

High-valent oxometal transients have been shown to mediate O—O bond formation *via* the nucleophilic attack of water/hydroxide or oxyl-radical coupling, resulting in the oxidation of water. An oxomanganese(V) species has also been proposed to be the active oxidant during the sunlight-driven oxidation of water by the biological oxygen-evolving complex (OEC). Enthused by the facile electrochemical oxidation of complex **1** to form oxomanganese complexes (**2-4**), we, therefore, set out to examine the efficacy of these high-valent oxomanganese complexes towards O—O bond formation by performing CV experiments using complex **1** in acetonitrile in the presence of added water. Indeed, the CVs of complex **1** in acetonitrile in the presence of different concentrations of water display a significant increase in the current near the potential for the third oxidation wave (**3**→**4**) (Figure 8). The CV scans indicate that the oxidation of the oxomanganese(V) species (**3**) to the formally Mn^{VI}(O) species (**4**) triggers electrocatalytic oxidation of water. The anodic and cathodic peak current of the Mn^{IV/III} couple varies linearly with the square root of scan rate ($v^{1/2}$) indicating a diffusion-controlled electron transfer process at the electrode (Figure S9). The catalytic peak current varies linearly with the catalyst concentration as well as with $[\text{H}_2\text{O}]^{1/2}$ (Figure S10) indicating first-order dependence of the rate of electrocatalysis on the concentrations of both complex **1** and added water. The peak intensity of the Mn(IV)/Mn(V) redox couple increases with $[\text{H}_2\text{O}]$, which suggests that the putative oxomanganese(V) complex can also oxidize water to some extent.

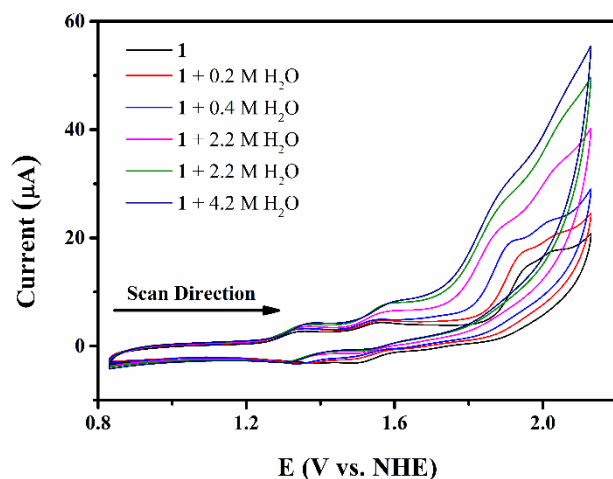


Figure 8. CVs of complex **1** (0.1 mM) with gradual addition of water in acetonitrile containing 0.1 M LiClO₄ at a scan rate of 100 mV/s.

Control potential electrolysis was conducted at a Fluorine doped tin oxide (FTO) electrode with a cell operating potential of 1.95 V vs. NHE in a two-compartment cell separated by a frit in an acetonitrile-water mixture (5%) (Figure S11) to quantify the products of water oxidation. Interestingly, oxygen bubbles were not detected during the CPE experiments. The amount of dissolved oxygen was measured using a Clark-type electrode and the analysis yielded a Faradaic efficiency of only 10% based on a four-electron process. The results indicate that oxidation of water via a $2e^-/2H^+$ pathway might be operative in the present case. To check this hypothesis, iodometric titration of the electrolyzed solution using acidified KI was performed and the characteristic peak of I_3^- was monitored by UV-vis spectroscopy. A total of 2.3 C charge was passed after 2 h of electrolysis and 4 μ mole of H₂O₂ was detected by the iodometric titration. Faradaic efficiency in the first 2h is, therefore, calculated to be ~30% (Figure S12). The lower Faradaic yield may be rationalized in terms of competitive reactions between the high-valent oxo-transient (**4**) and the coordinated ligand/organic solvent akin to what was proposed during electrocatalytic water oxidation by a synthetic tetranuclear Mn-cluster.⁴⁶ To intercept the full oxidizing potential of the putative species, additional CPE experiments were performed in the presence of 9,10-DHA (C—H BDE = 78 kcal mol⁻¹). Post CPE analysis revealed the formation of anthracene with 80% Faradaic efficiency and only a trace amount of H₂O₂. Consistent with the results, the Faradaic yield of H₂O₂ could be significantly improved using Rotating Ring Disc Electrode (RRDE) voltammetry technique.^{47,48} Thus, when the glassy carbon (GC) disc was scanned toward the anodic potential to catalyze water into hydrogen peroxide, the ring was poised at a constant potential of 0.6 V vs. Fc⁺/Fc to oxidize the generated hydrogen peroxide (Figure 9). Currents at both the electrodes were stable and the Faradaic efficiency was calculated to be 90 (\pm 20) % at 1.9 V from the ring (j_r) and disc current (j_d) using the equation 1,

$$\varepsilon = \frac{j_r}{Nj_d} \quad (1)$$

where, N is the collection efficiency which was calculated to be 0.22 in this case. The ring and disc currents were taken after background correction.

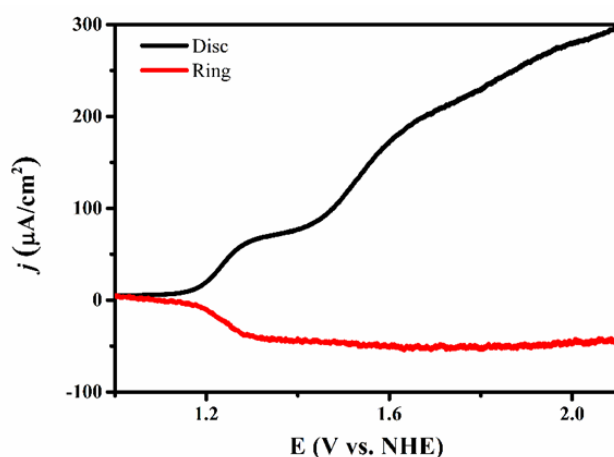


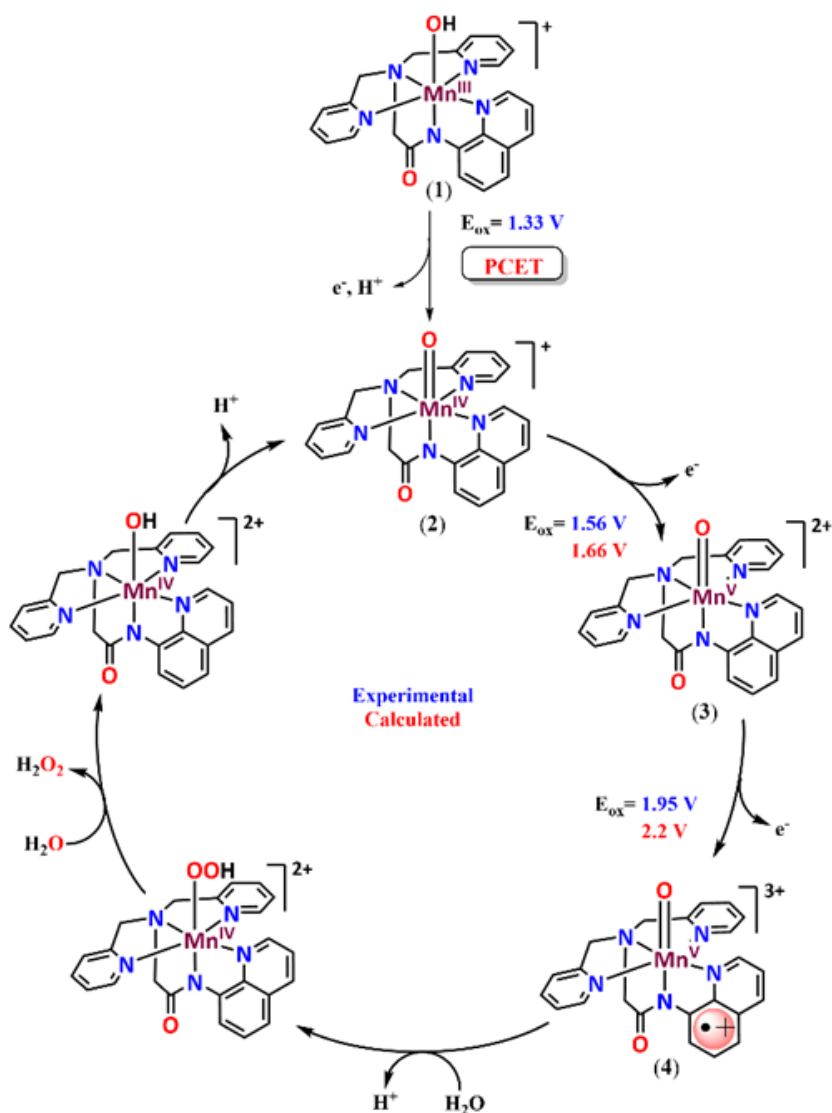
Figure 9. RRDE LSV of complex **1** (0.1 mM) for the detection of H_2O_2 in acetonitrile (10% water) using a GC disc and Pt ring electrode at a scan rate of 10 mV/s and rotation speed of 900 rpm. Pt ring was held at 0.6 V vs. Fc^+/Fc .

The homogeneity of the catalyst was tested under the electrochemical conditions in acetonitrile. After multiple scan cycles catalytic current was found to decrease with consecutive scans (Figure S13). The GC electrode was then successively rinsed with water and acetonitrile. The rinsed electrode in a catalyst-free fresh electrolyte solution exhibited no catalytic peak which excludes the possibility of the formation of redox active heterogeneous species (Figure S13). A similar rinsing test following the CPE using an FTO electrode also confirmed the absence of any catalytically active metal deposition (Figure S13).

Furthermore, to test the possibility of the formation of free Mn ions during electrocatalysis, additional CV experiments were performed in the presence of the chelating ligand, 2,2'-bipyridine. The addition of the chelating agent did not suppress the catalytic current (Figure S14). Under identical conditions, the CV of 0.5 mM $\text{Mn}(\text{ClO}_4)_2 \cdot 6\text{H}_2\text{O}$ did not show any catalytic activity which also emphasizes the fact that complex **1** is the active catalyst (Figure S15). Furthermore, the possibility of nanoparticle formation was ruled out based on dynamic light scattering measurements before and after the electrolysis (Figure S16). However, a 30% decrease in catalytic current from its initial value was observed after CPE indicating partial degradation of the active catalyst. The catalyst decomposition may in part, be rationalized in terms of the oxidation of the methylene groups of the coordinated ligand by the reactive high-valent oxomanganese(V/VI) transients. Nevertheless, the results indicate that despite lacking stability during electrochemical oxidations, complex **1** acts as a molecular complex under the experimental conditions.

Proposed Mechanism

Based on the electrochemical results and theoretical calculations discussed above, a mechanism of the formation of O—O bond is proposed (Scheme 2).



Scheme 2. Possible mechanism of electrocatalytic water oxidation catalyzed by **1** in acetonitrile-water. The experimental and computed redox potentials (vs NHE) are shown in blue and red, respectively.

In the catalytic cycle, the $[(\text{dpaq})\text{Mn}^{\text{III}}(\text{OH})]\text{ClO}_4$ (**1**) undergoes a $(1e^- + 1\text{H}^+)$ proton coupled electron transfer (PCET) process to form the oxomanganese(IV) intermediate, $[(\text{dpaq})\text{Mn}^{\text{IV}}(\text{O})]^+$ (**2**), consistent with the bulk electrolysis experiment at 1.45 V in acetonitrile (*vide supra*). Complex **2** undergoes another metal centred oxidation followed by a mixed metal-ligand centred oxidation process to generate the catalytically active intermediate, $[(\text{dpaq}^+)\text{Mn}^{\text{V}}(\text{O})]^{3+}$ (**4**). The resulting intermediate **4** is expected to react with water by a rate-limiting O—O bond formation process to generate an end-on hydroperoxide intermediate. Previous studies on metal complexes bearing anionic nitrogen *trans* to the substrate binding sites have been known to favor the formation of end-on peroxo complexes with H_2O_2 over the comparatively less reactive side-on peroxo intermediates.⁴⁹ Involvement of the formal Mn(VI) oxidation state in water oxidation finds relevance with the proposition by Zhang and Sun, who implicated the probable participation of Mn(VII)–dioxo species in the $S_3 \rightarrow S_4$ transition in the natural photosynthetic cycle.^{50, 51} Hydrolysis of the hydroperoxo ligand with the water facilitates the release of

H₂O₂ and generates the Mn(IV)-OH complex, which is rapidly converted to complex **2** in acetonitrile.⁴⁰ The sequence of events can, therefore, explain the formation of H₂O₂ during electrocatalytic water oxidation by **1** in acetonitrile.

Summary and Conclusion

In conclusion, the present study elucidates the electrochemical generation of high-valent oxomanganese transients, commencing from the hydroxomanganese(III) complex (**1**). The oxomanganese(IV) species (**2**), formed via PCET from **1**, was shown to accumulate during bulk electrolysis experiments at 1.45 V vs. NHE. This electrochemical approach, circumventing the need for chemical oxidants, redox-inactive metal ions, or protic acids, reinforces the previous claim that the oxomanganese(IV) transient is indeed 'unbound'. The results underscore an alternative pathway for the generation of the oxomanganese(IV) complex (**1**) without the requirement of redox-inactive metal ions or Brønsted acid additives as proposed earlier.³⁸⁻⁴⁰ Moreover, a detailed spectroelectrochemical study of **1** as a function of applied potential in the absence and presence of added water conclusively prove that the source of O-atom in **2** is the Mn(III)-OH precursor (**1**) and not the added water as argued in a recent study.³⁹ Additional one-electron oxidation events centred at 1.58 and 1.9 V vs. NHE are proposed to generate formally Mn(V)-oxo (**3**) and Mn(VI)-oxo (**4**) transients, respectively. Although these high-valent oxomanganese complexes could not be characterized, detailed theoretical investigation indicates a metal-based oxidation event at 1.58 V generating [(dpaq)Mn^V(O)]²⁺ (**3**). The theoretical results further indicate that the oxidation event at 1.9 V is a mixed metal-ligand centred, wherein the electron eliminates from an orbital composed of equitable contribution from metal and ligand, leaving a single electron in the quinoline-dominated orbital in the doublet ground spin state of complex **4**, where manganese exists in the formal and physical oxidation state of VI and V respectively. The mixed metal-ligand (quinoline)-based oxidation, therefore, is proposed to generate [(dpaq⁺)Mn^V(O)]³⁺ (**4**), a non-heme analogue of the species 'Compound I', that presumably reacts with water to install an O—O bond. In acetonitrile, complex **1** mediates the electrocatalytic water oxidation by 2e⁻/2H⁺ to form H₂O₂ with 90% Faradaic yield. The present work reinforces the idea that manganese complexes with terminal hydroxide ligand may play a key role in the O—O bond formation. Moreover, electrochemical access to highly reactive and hence undetectable high-valent Mn(V)-oxo (**3**) and Mn(VI)-oxo (**4**) transients opens us new avenues towards harnessing the oxidative potentials of these putative species for challenging C—H activation.

Experimental Section

General Methods

All the solvents and reagents were obtained from commercial sources and used as received unless mentioned otherwise. The ligand H-dpaq,⁵² [(dpaq)Mn^{III}(OH)](ClO₄)³⁷ and [Zn^{II}(dpaq)](ClO₄)²¹ were prepared according to the previously reported procedures. The solvents used for electrochemical studies

were purified following standard methods reported in the literature. All the electrodes and setup for electrochemical measurements were purchased from CH Instruments. Thermo Scientific™ Eutech™ CyberScan DO 600 Dissolved Oxygen Meter was used for oxygen measurements and Parkin-Elmer LAMBDA™ 265 UV/Vis spectrophotometer was used for recording the UV-Vis spectra. Raman spectra were measured with a Triple Raman spectrometer (Model T64000, Make J-Y Horiba) equipped with 1800 grooves/mm gratings, a TE cooled Synapse CCD detector, and an open stage Olympus microscope with a 50× objective. The samples were excited with a 532 nm wavelength (0.2 mW power, 20 s integration time, and 10 accumulations) laser from a DPSS Nd:YAG laser (Make: Spectra Physics). Labeling experiments were carried out with $^{18}\text{O}_2$ gas (99 atom %) or H_2^{18}O (98 atom %) purchased from Icon Services Inc., USA. Samples for recording Raman spectra were prepared by drop-casting an acetonitrile solution of the complex on a glass slide. GC-MS measurements were carried out with a PerkinElmer Clarus 680 GC and SQ8T MS using an Elite 5MS (30 m x 0.25 mm x 0.25 μm) column with a maximum temperature of 300°C.

Caution! Perchlorate salts of metal complexes with organic ligands are potentially explosive and should be handled with utmost care. Only small amounts of these materials were prepared. The $[(\text{dpaq})\text{Mn}^{\text{III}}(\text{OH})]^+$ complex can also be prepared by using $\text{Mn}(\text{II})(\text{OTf})_2$ instead of $\text{Mn}(\text{ClO}_4)_2$ ⁴¹ and use of perchlorate salts should be avoided whenever possible.

Electrochemistry

Electrochemical experiments were carried out using CH Instruments Model 700E Series Bipotentiostat. Rotating Ring Disk Electrochemistry (RRDE) experiments were performed using a 3A RRDE ALS BAS Japan model. All electrochemical measurements were performed at room temperature and cyclic voltammetry experiments were carried out using a three-electrode setup with automatic IR compensation. For experiments in acetonitrile, 0.1 M lithium perchlorate (LiClO_4) was used as a supporting electrolyte. All electrochemical experiments were performed using a three-electrode system where a glassy carbon (GC) electrode (diameter 3.00 mm, area 0.0707 cm^2) was used as the working electrode and Pt wire was used as the counter electrode as well as the reference electrode (unless mentioned otherwise) which was referenced externally with ferrocene. Before each experiment, the sample solutions were purged with nitrogen for 15 min and a stream of nitrogen was maintained over the solutions during experiments. For experiments in aqueous solutions, Ag/AgCl (satd. KCl) was used as a reference electrode. The volume of the electrolyte solution was kept constant during the experiments. The GC working electrode was rinsed with deionized water several times, polished with alumina slurry, and rinsed again with water before each use.

During controlled potential electrolysis (CPE) the electrolysis solution was stirred at a constant rotation speed.

For the experiments in acetonitrile, ferrocene/ferrocenium ($\text{Fc}^{0/+}$) redox couple was used as an internal reference and all voltammograms were referenced against the normal hydrogen electrode (NHE) following equation 2.⁵³

$$E (\text{vs. NHE}) = E (\text{vs. Fc}^{0/+}) + 0.63 \text{ V} \quad \text{eqn. 2}$$

In the experiments where Ag/AgCl (satd. KCl) was used as a reference electrode, the conversion to NHE was made by using the following equation,

$$E (\text{vs. NHE}) = E (\text{vs. Ag/AgCl}) + 0.199 \text{ V} \quad \text{eqn. 3}$$

Spectroelectrochemical experiments were performed at 298 K in a quartz cell (1.0 cm optical path length) equipped with a Platinum gauze (80 mesh, 6 mm × 7 mm), a Pt wire counter electrode, and Ag/AgCl in saturated KCl as the reference electrode. The cell was filled with the working solution and placed in a PerkinElmer Lambda 265 diode array spectrophotometer equipped with a Peltier-driven temperature controller.

Generation of $[(\text{dpaq})\text{Mn}^{\text{IV}}(\text{O})]^+$

A solution of complex **1** (1.0 mM) in 2.0 mL wet acetonitrile ($[\text{H}_2\text{O}] = 150 \text{ mM}$) containing 0.1 M LiClO_4 as the supporting electrolyte was taken in a spectroelectrochemical quartz cuvette (1.0 cm optical path length). The cell was then fitted with a Pt gauze (80 mesh, 6 mm × 7 mm), a Pt wire counter electrode, and Ag/AgCl in saturated KCl as the reference electrode and placed in a PerkinElmer Lambda 265 diode array spectrophotometer equipped with a Peltier-driven temperature controller. The electrodes were connected to the electrochemical workstation (CHI700E). Controlled potential experiments applying potential greater than 1.4 V vs. NHE resulted in the near quantitative conversion of **1** to **2** in 10 min, as confirmed by the appearance of the absorption features at 500 and 700 nm (Figure 2b).

Complex **2** was also synthesized electrochemically from **1** by bulk electrolysis in an SBC Bulk electrolysis cell (ALS Co., Ltd). A 90 mL 0.5 mM solution of **1** in wet acetonitrile containing 0.1 M LiClO_4 as the supporting electrolyte was introduced into the cell that was fitted with a porous carbon electrode (PCE) working electrode, Ag/AgCl in saturated KCl as the reference electrode and a Pt counter electrode. The counter electrode was separated by a glass frit. Controlled potential electrolysis (CPE) was carried out at 1.45 V vs. NHE and the solution was stirred at a constant rotation speed (400 rpm) with a stir bar. For UV-vis measurements, solutions were taken at different time intervals from the electrolysis chamber for analysis. Similar CPE experiments were also carried out in a two-compartment cell using a Fluorine doped tin oxide (FTO) plate (area = 2 cm²) as a working electrode and a Pt wire was used as both counter and reference electrode (Figure S3). The color of the solution turned green after electrolysis and the UV-Vis spectral analysis confirmed the generation of complex **2**.

Quantification of hydrogen peroxide

Hydrogen peroxide was quantified by modifying previous reports.⁵⁴⁻⁵⁶ The acetonitrile solution after bulk electrolysis was passed through a short silica column to remove the metal complex. To 5 mL of the colourless solution obtained by silica filtration was added 5 mL 1M KI in 0.05M H₂SO₄ and the mixture was left to stand for 5 min. After that, the solution was diluted with water and subjected to UV-vis spectral analysis. From the absorption spectrum of I³⁻ at 353 nm ($\epsilon = 26,000 \text{ M}^{-1}\text{cm}^{-1}$) the yield of hydrogen peroxide was calculated considering the dilution factor. A control experiment was also carried out under identical conditions with a solution which was not electrolyzed.

Note: the I³⁻ continues to develop because of slow background oxidation in the presence of air and it was made sure that the sample does not stand for more than 5 min.

Computational Methods

Calculations at the level of Density Functional Theory (DFT) and wave function based multiconfigurational self-consistent field (MCSCF) method have been performed to gain more insight into the electronic structure of the complex under investigation. The molecules are optimized with meta-hybrid TPSSh functional⁵⁷ and relativistic basis set implemented through zeroth-order regular approximation (ZORA)^{58,59} retaining one-centre terms and using ZORA-recontracted def2-TZVP basis sets for all elements other than C and H, for which ZORA-def2-SVP basis sets were used.⁶⁰ To eliminate any potential errors from the use of resolution of identity (RI) and chain-of-spheres (COSX) approximations to coulomb and exact exchange,⁶¹ a large decontracted SARC/J auxiliary basis set is used.⁶² Increased integration accuracy (Grid6, GridX8 and IntAcc 6.0 in ORCA convention) and tight SCF convergence criteria were applied. During optimization, the solvent effect is included as a dielectric medium through the conductor-like polarizable continuum model (CPCM).⁶³ Non-covalent interaction was taken into account by using atom-pairwise dispersion corrections with Becke-Johnson (D3BJ) damping.⁶⁴ In addition to the DFT, the multiconfigurational Complete Active Space Self Consistent Field (CASSCF)⁶⁵⁻⁶⁷ method has been adopted for in-depth inspection of electronic structure. Quasi-restricted orbitals from DFT calculation were used as initial guess for state-average CASSCF calculation. A total number of 10, 10, and 5 states has been considered for such state-average calculation for the quartet spin state of complex **2** (d^3 system), triplet spin state of complex **3** (d^2 system) and doublet spin state of complex **4** (d^1 system) respectively. These many numbers of roots, even for the ligand-orbital including active space, has been found sufficient to produce current electronic structure of the transition metal complexes.⁶⁸⁻⁷⁰ However, appropriate number of roots due to inclusion of ligand-based orbitals can be important in getting the correct ground spin state of the systems under investigation. Hence, we tried to perform CASSCF calculations with in-creased number of roots, but the computations could not be converged. All the CASSCF calculations were performed with consideration of scalar relativistic effect through ZORA with relativistic basis sets similar to the DFT calculations. The resolution of identity (RI) approximation was adopted with a def2-TZVP/C auxiliary basis set. Dynamic

correlation was recovered by employing the strongly contracted N -electron Valence Perturbation Theory up to second order (SC-NEVPT2).⁷¹ All the calculations are implemented in ORCA (version 4.2).⁷²

The oxidation potential for the redox events is calculated through the Nernst equation as,

$$E_{R/O}^0 = E_{SHE}^0 - \frac{\Delta G_{R/O}^0}{nF} \quad \text{eqn. 4}$$

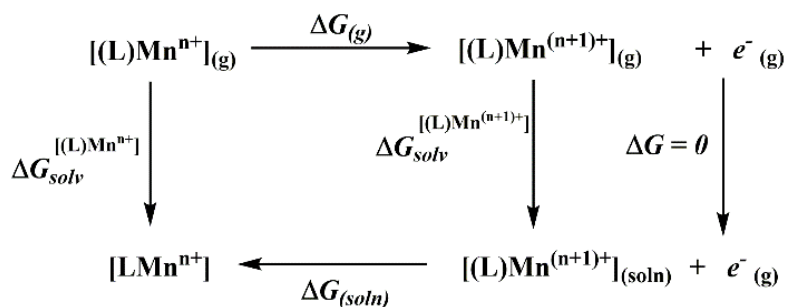
where the $\Delta G_{R/O}^0$ is the Gibbs free energy difference between the reductant and the oxidant in the acetonitrile solution, n being the number of electrons involved in the redox events ($n = 1$ in the present cases), and F is the Faraday constant, which is equal to the unit charge e in case the employed unit of energy is chosen to be eV . The superscript circle indicates the standard state of 1 atom ideal gas for gases and a standard state of 1 molal ideal solution for the solute.⁷³ The redox potential for the standard hydrogen electrode (E_{SHE}^0) is taken to be -4.43 eV,⁷⁴ which eliminates the need of calculating the free energy of proton/electron in solution.⁷⁵ The difference of the Gibbs free energy is calculated by using a thermodynamic (Born – Haber) cycle as depicted in the following scheme and the equation 5,^{76,77}

$$\Delta G_{R/O(soln)}^0 = IE(0K) + \Delta G_{trans,vib,rot,-TS}^0 + \Delta G_{solv}^0 \quad \text{eqn. 5}$$

Where $IE(0K)$ is the adiabatic ionization energy at 0 K with the consideration of zero-point vibrational energy (ZPVE)

$$IE(0K) = \Delta U_{elec} + ZPVE \quad \text{eqn. 6}$$

With ΔU_{elec} being the difference of total electronic energy between reductant and oxidant. The second and third term in equation 5 involves the thermal contribution of translational, vibrational, and rotational motion at 298 K and the stabilization by entropic contribution and the difference of solvation energy of oxidant and reductant. To include non-electrostatic contribution towards the free energy of solvation, the SMD model has been used in combination with CPCM.⁷⁸ However, to minimize errors in the treatment of solvation energies and entropic effects for the complexes **2**, **3** and **4**, similar calculation of redox potential for ferricenium (Fc⁺)/ferrocene(Fc) couple in acetonitrile with known redox potential (4.980 V) has been performed to estimate the error margin.^{79,80} The ferrocenium (Fc⁺)/ferrocene(Fc) couple is considered as an ideal reference against the first-row transition metal systems.⁸¹⁻⁸³ Thus, estimated error is used to refine the oxidation potentials for Mn(IV)/Mn(V) and Mn(V)/Mn(VI) couple (Table S2). Vibrational frequencies required to get the parameters in the thermodynamic cycle are obtained by frequency calculation of the involved species over their local minimum structure in solution, with the same DFT methodology, as adopted for geometry optimization.



Scheme 3. Thermodynamic cycle used for calculating redox potential.

Acknowledgement

This work was supported by grants from the Science and Industrial research Board (SERB, Project No(s). CRG/2021/002064 and YSS/2015/000829) to A.N.B. and Project No. 01(2926)/18/EMR-II to T.K.P.). Financial support for the procurement of the Electrochemical Workstation was provided by Technical Education Quality Improvement programme (TEQIP Phase III) of Government of India. S.P. thanks Max Planck Institute for Kohlenforschung and Indian Association for the Cultivation of Science for computational facility. NIT Sikkim is appreciated for allocating doctoral research fellowships to S.B. and S. N. C.

References

1. Amin, M.; Vogt, L.; Szejgis, W.; Vassiliev, S.; Brudvig, G. W.; Bruce, D.; Gunner, M. R. Proton-Coupled Electron Transfer During the S-State Transitions of the Oxygen-Evolving Complex of Photosystem II. *J. Phys. Chem. B* **2015**, *119*, 7366-7377.
2. Barry, B. A. Proton coupled electron transfer and redox active tyrosines in Photosystem II. *J. Photochem. Photobiol. B, Biol.* **2011**, *104*, 60-71.
3. Cox, N.; Lubitz, W. Molecular Concepts of Water Splitting: Nature's Approach. *GREEN* **2013**, *3*, 235-263.
4. Yano, J.; Kern, J.; Sauer, K.; Latimer, M. J.; Pushkar, Y.; Biesiadka, J.; Loll, B.; Saenger, W.; Messinger, J.; Zouni, A.; Yachandra, V. K. Where Water Is Oxidized to Dioxygen: Structure of the Photosynthetic Mn₄Ca Cluster. *Science* **2006**, *314*, 821.
5. Cox, N.; Pantazis, D. A.; Lubitz, W. Current Understanding of the Mechanism of Water Oxidation in Photosystem II and Its Relation to XFEL Data. *Ann. Rev. Biochem.* **2020**, *89*, 795-820.
6. Guo, Z.; Barry, B. A. Calcium, Ammonia, Redox-Active Tyrosine YZ, and Proton-Coupled Electron Transfer in the Photosynthetic Oxygen-Evolving Complex. *J. Phys. Chem. B* **2017**, *121*, 3987-3996.
7. Hammarström, L.; Styring, S. Proton-coupled electron transfer of tyrosines in Photosystem II and model systems for artificial photosynthesis: the role of a redox-active link between catalyst and photosensitizer. *Energy Environ. Sci.* **2011**, *4*, 2379-2388.

8. Keough, J. M.; Jenson, D. L.; Zuniga, A. N.; Barry, B. A. Proton Coupled Electron Transfer and Redox-Active Tyrosine Z in the Photosynthetic Oxygen-Evolving Complex. *J. Am. Chem. Soc.* **2011**, *133*, 11084-11087.
9. Costas, M.; Mehn, M. P.; Jensen, M. P.; Que, L. Dioxygen Activation at Mononuclear Nonheme Iron Active Sites: Enzymes, Models, and Intermediates. *Chem. Rev.* **2004**, *104*, 939-986.
10. Nam, W. Dioxygen Activation by Metalloenzymes and Models. *Acc. Chem. Res.* **2007**, *40*, 465-465.
11. Cox, N.; Pantazis, D. A.; Neese, F.; Lubitz, W. Biological Water Oxidation. *Acc. Chem. Res.* **2013**, *46*, 1588-1596.
12. Cox, N.; Retegan, M.; Neese, F.; Pantazis, D. A.; Boussac, A.; Lubitz, W. Electronic structure of the oxygen-evolving complex in photosystem II prior to O-O bond formation. *Science* **2014**, *345*, 804.
13. Siegbahn, P. E. M. Structures and Energetics for O₂ Formation in Photosystem II. *Acc. Chem. Res.* **2009**, *42*, 1871-1880.
14. Guo, M.; Corona, T.; Ray, K.; Nam, W. Heme and Nonheme High-Valent Iron and Manganese Oxo Cores in Biological and Abiological Oxidation Reactions. *ACS Cen. Sci.* **2019**, *5*, 13-28.
15. Kal, S.; Xu, S.; Que Jr, L. Bio-inspired Nonheme Iron Oxidation Catalysis: Involvement of Oxoiron(V) Oxidants in Cleaving Strong C-H Bonds. *Angew. Chem., Int. Ed.* **2020**, *59*, 7332-7349.
16. Ray, K.; Pfaff, F. F.; Wang, B.; Nam, W. Status of Reactive Non-Heme Metal-Oxygen Intermediates in Chemical and Enzymatic Reactions. *J. Am. Chem. Soc.* **2014**, *136*, 13942-13958.
17. Blakemore, J. D.; Crabtree, R. H.; Brudvig, G. W. Molecular Catalysts for Water Oxidation. *Chem. Rev.* **2015**, *115*, 12974-13005.
18. Shaffer, D. W.; Xie, Y.; Concepcion, J. J. O-O bond formation in ruthenium-catalyzed water oxidation: single-site nucleophilic attack vs. O-O radical coupling. *Chem. Soc. Rev.* **2017**, *46*, 6170-6193.
19. Das, D.; Pattanayak, S.; Singh, K. K.; Garai, B.; Sen Gupta, S. Electrocatalytic water oxidation by a molecular cobalt complex through a high valent cobalt oxo intermediate. *Chem. Commun.* **2016**, *52*, 11787-11790.
20. Liu, Y.; Su, X.; Guan, W.; Yan, L. Ruthenium-based catalysts for water oxidation: the key role of carboxyl groups as proton acceptors. *Phys. Chem. Chem. Phys.* **2020**, *22*, 5249-5254.
21. Biswas, S.; Bose, S.; Debgupta, J.; Das, P.; Biswas, A. N. Redox-active ligand assisted electrocatalytic water oxidation by a mononuclear cobalt complex. *Dalton Trans.* **2020**, *49*, 7155-7165.
22. Lee, H.; Wu, X.; Sun, L. Homogeneous Electrochemical Water Oxidation at Neutral pH by Water-Soluble Ni^{II} Complexes Bearing Redox Non-innocent Tetraamido Macrocyclic Ligands. *ChemSusChem* **2020**, *13*, 3277-3282.
23. Matheu, R.; Garrido-Barros, P.; Gil-Sepulcre, M.; Ertem, M. Z.; Sala, X.; Gimbert-Suriñach, C.; Llobet, A. The development of molecular water oxidation catalysts. *Nat. Rev. Chem.* **2019**, *3*, 331-341.

24. Pattanayak, S.; Chowdhury, D. R.; Garai, B.; Singh, K. K.; Paul, A.; Dhar, B. B.; Gupta, S. S. Electrochemical Formation of Fe^V(O) and Mechanism of Its Reaction with Water During O–O Bond Formation. *Chem. Eur. J.* **2017**, *23*, 3414-3424.
25. Chandra, B.; K. M, H.; Pattanayak, S.; Gupta, S. S. Oxoiron(v) mediated selective electrochemical oxygenation of unactivated C–H and C–C bonds using water as the oxygen source. *Chem. Sci.* **2020**, *11*, 11877-11885.
26. Das, A.; Nutting, J. E.; Stahl, S. S. Electrochemical C–H oxygenation and alcohol dehydrogenation involving Fe-oxo species using water as the oxygen source. *Chem. Sci.* **2019**, *10*, 7542-7548.
27. de Sousa, D. P.; Miller, C. J.; Chang, Y.; Waite, T. D.; McKenzie, C. J. Electrochemically Generated cis-Carboxylato-Coordinated Iron(IV) Oxo Acid–Base Congeners as Promiscuous Oxidants of Water Pollutants. *Inorg. Chem.* **2017**, *56*, 14936-14947.
28. Nishida, Y.; Morimoto, Y.; Lee, Y.-M.; Nam, W.; Fukuzumi, S. Effects of Proton Acceptors on Formation of a Non-Heme Iron(IV)–Oxo Complex via Proton-Coupled Electron Transfer. *Inorg. Chem.* **2013**, *52*, 3094-3101.
29. Collins, M. J.; Ray, K.; Que, L. Electrochemical Generation of a Nonheme Oxoiron(IV) Complex. *Inorg. Chem.* **2006**, *45*, 8009-8011.
30. Coggins, M. K.; Zhang, M.-T.; Vannucci, A. K.; Dares, C. J.; Meyer, T. J. Electrocatalytic Water Oxidation by a Monomeric Amidate-Ligated Fe(III)–Aqua Complex. *J. Am. Chem. Soc.* **2014**, *136*, 5531-5534.
31. Kotani, H.; Suenobu, T.; Lee, Y.-M.; Nam, W.; Fukuzumi, S. Photocatalytic Generation of a Non-Heme Oxoiron(IV) Complex with Water as an Oxygen Source. *J. Am. Chem. Soc.* **2011**, *133*, 3249-3251.
32. Chandra, B.; Singh, K. K.; Gupta, S. S. Selective photocatalytic hydroxylation and epoxidation reactions by an iron complex using water as the oxygen source. *Chem. Sci.* **2017**, *8*, 7545-7551.
33. Lassalle-Kaiser, B.; Hureau, C.; Pantazis, D. A.; Pushkar, Y.; Guillot, R.; Yachandra, V. K.; Yano, J.; Neese, F.; Anxolabéhère-Mallart, E. Activation of a water molecule using a mononuclear Mn complex: from Mn-aquo, to Mn-hydroxo, to Mn-oxyl via charge compensation. *Energy Environ. Sci.* **2010**, *3*, 924-938.
34. Parsell, T. H.; Behan, R. K.; Green, M. T.; Hendrich, M. P.; Borovik, A. S., Preparation and Properties of a Monomeric MnIV-Oxo Complex. *J. Am. Chem. Soc.* **2006**, *128*, 8728-8729.
35. Lassalle-Kaiser, B.; Hureau, C.; Pantazis, D. A.; Pushkar, Y.; Guillot, R.; Yachandra, V. K.; Yano, J.; Neese, F.; Anxolabehere-Mallart, E. Activation of a water molecule using a mononuclear Mn complex: from Mn-aquo, to Mn-hydroxo, to Mn-oxyl via charge compensation. *Energy Environ. Sci.* **2010**, *3*, 924-938.
36. El Ghachtouli, S.; Lassalle-Kaiser, B.; Dorlet, P.; Guillot, R.; Anxolabehere-Mallart, E.; Costentin, C.; Aukauloo, A. Implications of remote water molecules on the electron transfer coupled processes at a nonporphyrinic Mn(III)-hydroxido complex. *Energy Environ. Sci.* **2011**, *4*, 2041-2044.

37. Biswas, S.; Mitra, A.; Banerjee, S.; Singh, R.; Das, A.; Paine, T. K.; Bandyopadhyay, P.; Paul, S.; Biswas, A. N. A High Spin Mn(IV)-Oxo Complex Generated via Stepwise Proton and Electron Transfer from Mn(III)-Hydroxo Precursor: Characterization and C-H Bond Cleavage Reactivity. *Inorg. Chem.* **2019**, *58*, 9713-9722.
38. Sankaralingam, M.; Lee, Y.-M.; Pineda-Galvan, Y.; Karmalkar, D. G.; Seo, M. S.; Jeon, S. H.; Pushkar, Y.; Fukuzumi, S.; Nam, W. Redox Reactivity of a Mononuclear Manganese-Oxo Complex Binding Calcium Ion and Other Redox-Inactive Metal Ions. *J. Am. Chem. Soc.* **2019**, *141*, 1324-1336.
39. Karmalkar, D. G.; Sankaralingam, M.; Seo, M. S.; Ezhov, R.; Lee, Y.-M.; Pushkar, Y. N.; Kim, W.-S.; Fukuzumi, S.; Nam, W. A High-Valent Manganese(IV)-Oxo-Cerium(IV) Complex and Its Enhanced Oxidizing Reactivity. *Angew. Chem., Int. Ed.* **2019**, *58*, 16124-16129.
40. Karmalkar, D. G.; Seo, M. S.; Lee, Y.-M.; Kim, Y.; Lee, E.; Sarangi, R.; Fukuzumi, S.; Nam, W. Deeper Understanding of Mononuclear Manganese(IV)-Oxo Binding Brønsted and Lewis Acids and the Manganese(IV)-Hydroxide Complex. *Inorg. Chem.* **2021**, *60*, 16996-17007.
41. Rice, D. B.; Jones, S. D.; Douglas, J. T.; Jackson, T. A. NMR Studies of a MnIII-hydroxo Adduct Reveal an Equilibrium between MnIII-hydroxo and μ -Oxodimanganese(III,III) Species. *Inorg. Chem.* **2018**, *57*, 7825-7837.
42. Rohner, S. S.; Kinzel, N. W.; Werlé, C.; Leitner, W. Systematic ligand variation to modulate the electrochemical properties of iron and manganese complexes. *Dalton Trans.* **2019**, *48*, 13205-13211.
43. Chowdhury, S. N.; Biswas, S.; Das, P.; Paul, S.; Biswas, A. N. Oxygen Reduction Assisted by the Concert of Redox Activity and Proton Relay in a Cu(II) Complex. *Inorg. Chem.* **2020**, *59*, 14012-14022.
44. Jung, C. The mystery of cytochrome P450 Compound I: A mini-review dedicated to Klaus Ruckpaul. *Biochim Biophys Acta Proteins Proteom.* **2011**, *1814*, 46-57.
45. Rittle, J.; Green, M. T. Cytochrome P450 Compound I: Capture, Characterization, and C-H Bond Activation Kinetics. *Science* **2010**, *330*, 933.
46. Han, Z.; Horak, K. T.; Lee, H. B.; Agapie, T. Tetranuclear Manganese Models of the OEC Displaying Hydrogen Bonding Interactions: Application to Electrocatalytic Water Oxidation to Hydrogen Peroxide. *J. Am. Chem. Soc.* **2017**, *139*, 9108-9111.
47. Liu, Y.; Han, Y.; Zhang, Z.; Zhang, W.; Lai, W.; Wang, Y.; Cao, R. Low overpotential water oxidation at neutral pH catalyzed by a copper(ii) porphyrin. *Chem. Sci.* **2019**, *10*, 2613-2622.
48. Mondal, B.; Chattopadhyay, S.; Dey, S.; Mahammed, A.; Mitra, K.; Rana, A.; Gross, Z.; Dey, A. Elucidation of Factors That Govern the $2e^-/2H^+$ vs $4e^-/4H^+$ Selectivity of Water Oxidation by a Cobalt Corrole. *J. Am. Chem. Soc.* **2020**, *142*, 21040-21049.
49. Annaraj, J.; Cho, J.; Lee, Y.-M.; Kim, S. Y.; Latifi, R.; de Visser, S. P.; Nam, W. Structural Characterization and Remarkable Axial Ligand Effect on the Nucleophilic Reactivity of a Nonheme Manganese(III)-Peroxo Complex. *Angew. Chem., Int. Ed.* **2009**, *48*, 4150-4153.
50. Zhang, B.; Daniel, Q.; Fan, L.; Liu, T.; Meng, Q.; Sun, L. Identifying MnVII-oxo Species during Electrochemical Water Oxidation by Manganese Oxide. *iScience* **2018**, *4*, 144-152.

51. Zhang, B.; Sun, L. Why nature chose the Mn₄CaO₅ cluster as water-splitting catalyst in photosystem II: a new hypothesis for the mechanism of O–O bond formation. *Dalton Trans.* **2018**, *47*, 14381-14387.
52. Hitomi, Y.; Arakawa, K.; Funabiki, T.; Kodera, M. An Iron(III)–Monoamidate Complex Catalyst for Selective Hydroxylation of Alkane C–H Bonds with Hydrogen Peroxide. *Angew. Chem., Int. Ed.* **2012**, *51*, 3448-3452.
53. Pavlishchuk, V. V.; Addison, A. W. Conversion constants for redox potentials measured versus different reference electrodes in acetonitrile solutions at 25°C. *Inorg. Chim. Acta* **2000**, *298*, 97-102.
54. Ackermann, J.; Meyer, F.; Kaifer, E.; Pritzkow, H. Tuning the Activity of Catechol Oxidase Model Complexes by Geometric Changes of the Dicopper Core. *Chem. Eur. J.* **2002**, *8*, 247-258.
55. Kadassery, K. J.; Dey, S. K.; Cannella, A. F.; Surendhran, R.; Lacy, D.C. Photochemical Water-Splitting with Organomanganese Complexes. *Inorg. Chem.* **2017**, *56*, 9954-9965.
56. Monzani, E.; Quinti, L.; Perotti, A.; Casella, L.; Gullotti, M.; Randaccio, L.; Geremia, S.; Nardin, G.; Faleschini, P.; Tabbì, G. Tyrosinase Models. Synthesis, Structure, Catechol Oxidase Activity, and Phenol Monooxygenase Activity of a Dinuclear Copper Complex Derived from a Triamino Pentabenzimidazole Ligand. *Inorg. Chem.* **1998**, *37*, 553-562.
57. Staroverov, V. N.; Scuseria, G. E.; Tao, J.; Perdew, J. P. Comparative assessment of a new nonempirical density functional: Molecules and hydrogen-bonded complexes. *J. Chem. Phys.* **2003**, *119*, 12129-12137.
58. van Lenthe, E.; Baerends, E. J.; Snijders, J. G. Relativistic total energy using regular approximations. *J. Chem. Phys.* **1994**, *101*, 9783-9792.
59. van Lenthe, E.; Snijders, J. G.; Baerends, E. J. The zero-order regular approximation for relativistic effects: The effect of spin–orbit coupling in closed shell molecules. *J. Chem. Phys.* **1996**, *105*, 6505-6516.
60. Pantazis, D. A.; Chen, X.-Y.; Landis, C. R.; Neese, F. All-Electron Scalar Relativistic Basis Sets for Third-Row Transition Metal Atoms. *J. Chem. Theory Comput.* **2008**, *4*, 908-919.
61. Neese, F.; Wennmohs, F.; Hansen, A.; Becker, U. Efficient, approximate and parallel Hartree–Fock and hybrid DFT calculations. A ‘chain-of-spheres’ algorithm for the Hartree–Fock exchange. *Chem. Phys.* **2009**, *356*, 98-109.
62. Weigend, F. Accurate Coulomb-fitting basis sets for H to Rn. *Phys. Chem. Chem. Phys.* **2006**, *8*, 1057-1065.
63. Cossi, M.; Rega, N.; Scalmani, G.; Barone, V. Energies, structures, and electronic properties of molecules in solution with the C-PCM solvation model. *J. Comput. Chem.* **2003**, *24*, 669-681.
64. Grimme, S.; Ehrlich, S.; Goerigk, L. Effect of the damping function in dispersion corrected density functional theory. *J. Comput. Chem.* **2011**, *32*, 1456-1465.
65. Roos, B. O.: The Complete Active Space Self-Consistent Field Method and its Applications in Electronic Structure Calculations. In *Advances in Chemical Physics*, 1987; pp 399-445.

66. Roos, B. O.; Taylor, P. R.; Sigbahn, P. E. M. A complete active space SCF method (CASSCF) using a density matrix formulated super-CI approach. *Chem. Phys.* **1980**, *48*, 157-173.
67. Ruedenberg, K.; Cheung, L. M.; Elbert, S. T. MCSCF optimization through combined use of natural orbitals and the brillouin–levy–berthier theorem. *Int. J. Quantum Chem.* **1979**, *16*, 1069-1101.
68. Sen, A.; Rajaraman, G., Can you break oxo-wall? – A multiconfigurational perspective. *Faraday Discussions.* **2022**, *234*, 175-194.
69. Chang, H.C.; Mondal, B.; Fang, H.; Neese, F.; Bill, E.; Ye, S., Electron Paramagnetic Resonance Signature of Tetragonal Low Spin Iron(V)-Nitrido and -Oxo Complexes Derived from the Electronic Structure Analysis of Heme and Non-Heme Archetypes, *J. Am. Chem. Soc.* **2019**, *141*, 2421 – 2434.
70. Mondal, B.; Neese, F.; Bill, E.; Ye, S. Electronic Structure Contributions of Non-Heme Oxo-Iron(V) Complexes to the Reactivity, *J. Am. Chem. Soc.* **2018**, *140*, 9531 – 9544.
71. Angeli, C.; Cimiraglia, R.; Evangelisti, S.; Leininger, T.; Malrieu, J. P. Introduction of n-electron valence states for multireference perturbation theory. *J. Chem. Phys.* **2001**, *114*, 10252-10264.
72. Neese, F. Software update: the ORCA program system, version 4.0. *WIREs Comput. Mol. Sci.* **2018**, *8*, e1327.
73. Isegawa, M.; Neese, F.; Pantazis, D. A. Ionization Energies and Aqueous Redox Potentials of Organic Molecules: Comparison of DFT, Correlated ab Initio Theory and Pair Natural Orbital Approaches. *J. Chem. Theory Comput.* **2016**, *12*, 2272-2284.
74. Reiss, H.; Heller, A. The absolute potential of the standard hydrogen electrode: a new estimate. *J. Phys. Chem.* **1985**, *89*, 4207-4213.
75. Solis, B. H.; Hammes-Schiffer, S. Computational Study of Anomalous Reduction Potentials for Hydrogen Evolution Catalyzed by Cobalt Dithiolene Complexes. *J. Am. Chem. Soc.* **2012**, *134*, 15253 – 15256.
76. Li, J.; Fisher, C. L.; Chen, J. L.; Bashford, D.; Noodleman, L. Calculation of Redox Potentials and pKa Values of Hydrated Transition Metal Cations by a Combined Density Functional and Continuum Dielectric Theory. *Inorg. Chem.* **1996**, *35*, 4694-4702.
77. Puzzolo, J. L.; Drusin, S. I.; Daier, V. A.; Signorella, S.; Moreno, D. M. Using theoretical calculations to predict the redox potential of mononuclear manganese complexes. *New J. Chem.* **2018**, *42*, 14827-14831.
78. Marenich, A. V.; Cramer, C. J.; Truhlar, D. G. Universal Solvation Model Based on Solute Electron Density and on a Continuum Model of the Solvent Defined by the Bulk Dielectric Constant and Atomic Surface Tensions. *J. Phys. Chem. B* **2009**, *113*, 18, 6378-6396.
79. Namazian, M.; Lin, C. Y.; Coote, M. L. Benchmark Calculations of Absolute Reduction Potential of Ferricinium/Ferrocene Couple in Nonaqueous Solutions. *J. Chem. Theory Comput.* **2010**, *6*, 9, 2721-2725.

80. Konezny, S. J.; Doherty, M. D.; Luca, O. R.; Crabtree, R. H.; Soloveichik, G. L.; Batista, V. S. Reduction of Systematic Uncertainty in DFT Redox Potentials of Transition-Metal Complexes. *J. Phys. Chem. C* **2012**, *116*, 10, 6349-6356.
81. Castro, L.; Bühl, M. Calculations of One-Electron Redox Potentials of Oxoiron(IV) Porphyrin Complexes. *J. Chem. Theory Comput.* **2014**, *10*, 1, 243-251.
82. Gritzner, G.; Kuta, J. Recommendations on Reporting Electrode Potentials in Nonaqueous Solvents (Recommendations 1983). *Pure Appl. Chem.* **1984**, *56*, 461-466.
83. Konezny, S. J.; Doherty, M. D.; Luca, O. R.; Crabtree, R. H.; Soloveichik, G. L.; Batista, V. S. Reduction of Systematic Uncertainty in DFT Redox Potentials of Transition-Metal Complexes. *J. Phys. Chem. C* **2012**, *116*, 10, 6349-6356.